micromachines

Article

Design and Analysis of Lithium–Niobate-Based Laterally Excited Bulk Acoustic Wave Resonator with Pentagon Spiral Electrodes

Ying Xie [1], Wenjuan Liu [1,2], Yao Cai [1,2], Zhiwei Wen [1], Tiancheng Luo [1], Yan Liu [1,*] and Chengliang Sun [1,2,*]

[1] The Institute of Technological Sciences, Wuhan University, Wuhan 430072, China
[2] Hubei Yangtze Memory Laboratories, Wuhan 430205, China
* Correspondence: liuyan92@whu.edu.cn (Y.L.); sunc@whu.edu.cn (C.S.)

Abstract: In this paper, we present a comprehensive study on the propagation and dispersion characteristics of A_1 mode propagating in Z-cut $LiNbO_3$ membrane. The A_1 mode resonators with pentagon spiral electrodes utilizing Z-cut lithium niobate ($LiNbO_3$) thin film are designed and fabricated. The proposed structure excites the A_1 mode waves in both *x*- and *y*-direction by utilizing both the piezoelectric constants e_{24} and e_{15} due to applying voltage along both the *x*- and *y*-direction by arranging pentagon spiral electrode. The fabricated resonator operates at 5.43 GHz with no spurious mode and effective electromechanical coupling coefficient (K^2_{eff}) of 21.3%, when the width of electrode is 1 µm and the pitch is 5 µm. Moreover, we present a comprehensive study of the effect of different structure parameters on resonance frequency and K^2_{eff} of XBAR. The K^2_{eff} keeps a constant with varied thickness of $LiNbO_3$ thin film and different electrode rotation angles, while it declines with the increase of *p* from 5 to 20 µm. The proposed XBAR with pentagon spiral electrodes realize high frequency response with no spurious mode and tunable K^2_{eff}, which shows promising prospects to satisfy the needs of various 5 G high-band application.

Keywords: XBAR; $LiNbO_3$ thin film; effective electromechanical coupling coefficient

check for updates

Citation: Xie, Y.; Liu, W.; Cai, Y.; Wen, Z.; Luo, T.; Liu, Y.; Sun, C. Design and Analysis of Lithium–Niobate-Based Laterally Excited Bulk Acoustic Wave Resonator with Pentagon Spiral Electrodes. *Micromachines* **2023**, *14*, 552. https://doi.org/10.3390/mi14030552

Academic Editors: Junhui Hu and Ming Yang

Received: 6 February 2023
Revised: 23 February 2023
Accepted: 24 February 2023
Published: 26 February 2023

1. Introduction

In recent years, with the explosion of mobile data from video streaming, virtual reality, and wireless communication, the needs for high frequency and large bandwidth of radio-frequency (RF) components have increased dramatically [1–3]. Nowadays, the surface acoustic wave (SAW) resonator and the thin film bulk acoustic wave resonators (FBARs) have dominated the market due to the excellent performances. However, there are obstacles for them to be used to high-frequency and large-bandwidth RF front-end devices. On the one hand, the effective electromechanical coupling coefficient (K^2_{eff}) of both SAW and FBAR are limited to 6–13% with aluminium nitride (AlN) thin film, not satisfying the demand of the relative bandwidth of filter above 6%, such as band N77 and N79. On the other hand, the SAW resonators and FBARs are difficult to operate above 5 GHz. The frequency of SAW hardly amounts to 3.5 GHz due to the limitation of acoustic velocity and the lithography technology. For FBAR, the thinner the piezoelectric film, the higher the frequency. However, the thinner thickness of piezoelectric film may cause the degradation of film crystal quality, which eventually influences the performance of devices [4–6].

In recent years, the laterally excited bulk acoustic resonator (XBAR) devices based on lithium niobate ($LiNbO_3$) thin film have been extensively studied as promising candidates for the application in fifth generation mobile communication [7–11]. XBARs can achieve a high frequency of more than 5 GHz, and a large K^2_{eff} of more than 20%, exceeding the traditional FBARs and SAW resonators due to the larger piezoelectric coefficients e_{15} and e_{24} of $LiNbO_3$. In 2019, V. Plessky et al. first presented a 4.8 GHz XBAR based on Z-cut $LiNbO_3$ thin film with a K^2_{eff} of 25%, showing the possibility of its application to filters in

the 3–6 GHz range [12]. In 2020, Ruochen Lu presented XBAR in 128° Y-cut $LiNbO_3$ thin films with the K^2_{eff} of 46.4%, which obtained the highest value of K^2_{eff} [13]. In 2021, Bohua Peng designed and fabricated a solid-mounted-type XBAR on ZY- $LiNbO_3$, operating at 5 GHz, to improve heat dissipation and temperature coefficient of frequency (TCF) [14].

The K^2_{eff} of resonator has a significant influence on the bandwidth of filters, and it can be adjusted by structural optimization and tuning piezoelectric coefficients. For example, Gianluca Piazza investigated the influence of the electrical boundary conditions of Lamb wave resonator imposed by the excitation electrodes on the K^2_{eff}, and determined that K^2_{eff} can be tuned with a varying range from 3% to 7% [15]. Jie Zou investigated the impact of Euler angle of $LiNbO_3$ film on the K^2_{eff} of the resonator. The K^2_{eff} varies largely due to the prominent anisotropy of the piezoelectric matrix, so the optimal cut angle can be chosen so as to optimize the K^2_{eff} [16]. Compared with Lamb wave resonator, the research on the structure and vibrate modes of XBAR is relatively immature, and there is almost no systematical analysis of the effect of XBAR structure parameters on the K^2_{eff}.

In this paper, we present a comprehensive study on the propagation characteristics of the plate modes propagating in Z-cut $LiNbO_3$ membrane. Then, we propose new pentagon spiral electrode structure to excite the A_1 mode in the $LiNbO_3$ thin film. The dependance of K^2_{eff} with the electrode rotation angle and the pitch of electrodes are investigated. A series of XBARs with pentagon spiral electrodes with different electrode pitches are fabricated. The resonance frequency of fabricated device is around 5.4 GHz, and the K^2_{eff} of the fabricated devices varied with the electrode pitch, corresponding to the results of simulations. The resonator with pentagon spiral electrodes operates at 5.4 GHz with tunable K^2_{eff}, showing promising prospect for application in super high-frequency RF front-end filters.

2. Design and Simulation

A. Propagation characteristics of plate mode

The plate waves propagating in the $LiNbO_3$ thin film include either the symmetric and antisymmetric Lamb wave (S_0, S_1, A_0 and A_1) or the plate shear wave (SH_0 and SH_1). XBAR consists of a suspended $LiNbO_3$ thin film with interdigital electrodes (IDEs) on top. When applying a voltage, with the generated lateral electric field in the electrode arrangement direction, shear antisymmetric A_1 mode is generated. To more accurately capture the A_1 mode propagation characteristics in Z-cut $LiNbO_3$ thin film, the three-dimensional eigenfrequency simulation is set up to calculate the open phase velocity (v_p) and the coupling coefficient (k^2) dispersion of the plate waves propagating in the piezoelectric membrane [17–19]. The v_p characteristics are the open-surface phase velocity and are calculated by Formula (1), and k^2 characteristics are calculated by Formula (2):

$$v_p = f \times \lambda, \tag{1}$$

$$k^2 = \frac{v_p^2 - v_m^2}{v_p^2}, \tag{2}$$

where f is the eigenfrequency of the acoustic mode obtained by the FEM simulation, λ is the length of the acoustic mode, and the v_m is the short-surface phase velocity calculated by FEM approach. In the simulation, the model is a 3D building block of the $LiNbO_3$ plate with period boundary conditions on both x- and y-directions. The IDTs are assumed to be infinitely thin with no material assigned, which means the mechanical loading is ignored and only electrical boundary conditions considered herein.

Figure 1 depicts the mode shapes of the six plate modes. The displacement profile or the mechanical vibration of the Lamb wave modes is in the propagation xz-plane, and for the SH plate modes in the sagittal yz-plane. The v_p and k^2 dispersion characteristics of six plate waves propagating in the Z-cut $LiNbO_3$ membrane are shown in Figure 2, where the h_{LiNbO3} is the thickness of $LiNbO_3$ membrane and λ represents the length of acoustic wave. Obviously, higher plate wave modes exhibit large v_p with strong dispersion

especially when the $h_{\mathrm{LiNbO3}}/\lambda$ is small, and high v_p is generally favored for high frequency applications. As shown in Figure 2b, the frequencies of higher plate modes stop scaling with β, rather depending solely on the plate thickness. This indicates that for the A_1 mode at low $h_{\mathrm{LiNbO3}}/\lambda$, the frequency is not pitch-controlled any more but thickness-controlled, which breaks the limit of lithography technology to frequency. High v_p beyond 40,000 m/s and large k^2 of higher than 30% can be obtained as $h_{\mathrm{LiNbO3}}/\lambda < 0.1$, making the feasibility of wideband operating in 6G bands using A_1 mode resonators in Z-cut $LiNbO_3$.

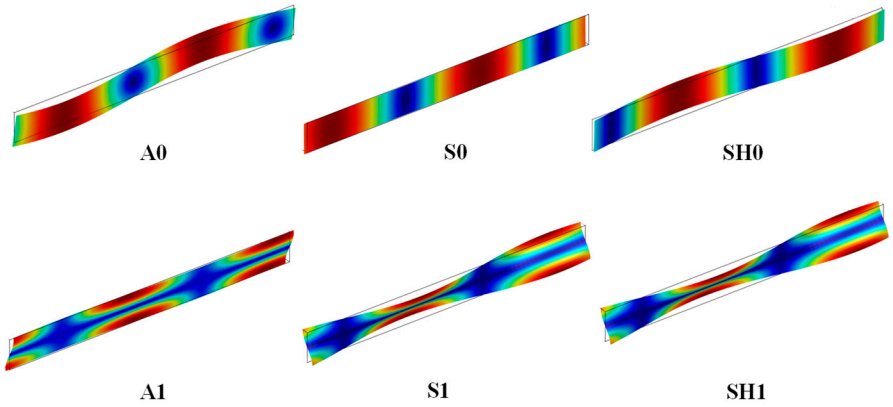

Figure 1. Schematic of the mode shapes of the first six plate modes (Lamb modes: A_0, S_0, A_1, S_1, and SH plate modes: SH_0 and SH_1) propagating in the Z-cut $LiNbO_3$ membrane when $h_{\mathrm{LiNbO3}}/\lambda = 0.1$.

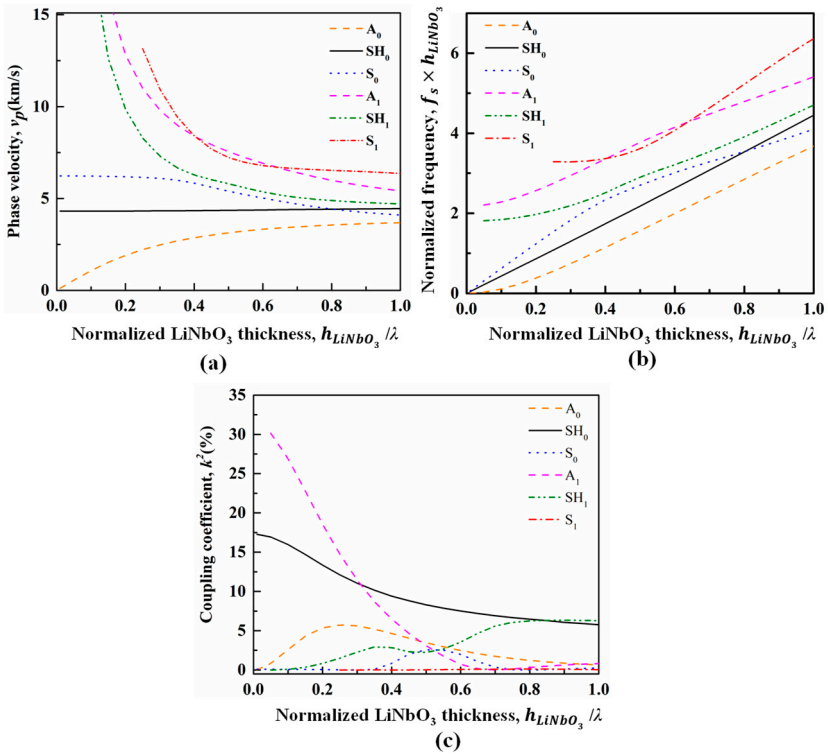

Figure 2. Calculated (**a**) dispersive phase velocities, (**b**) f-β dispersion curve, and (**c**) dispersive coupling coefficients of the first six plate modes in the Z-cut $LiNbO_3$ membrane.

B. Resonator design

The proposed XBAR with pentagon spiral shape electrode is illustrated in Figure 3a. The pentagon spiral electrodes are arranged alternatively on the top of Z-cut $LiNbO_3$ thin film, with two thin anchors connecting to the Ground–Signal–Ground (GSG) pads. The

electrical potentials are alternatingly applied to adjacent electrodes, as illustrated by "+" and "−" signs indicated in Figure 3, creating electric fields along both the x-direction and y-direction. The A-A′ cross-section view of the resonator is shown in Figure 3b, and an air cavity is formed underneath the $LiNbO_3$ thin film via backside release silicon substrate and silicon dioxide (SiO_2).

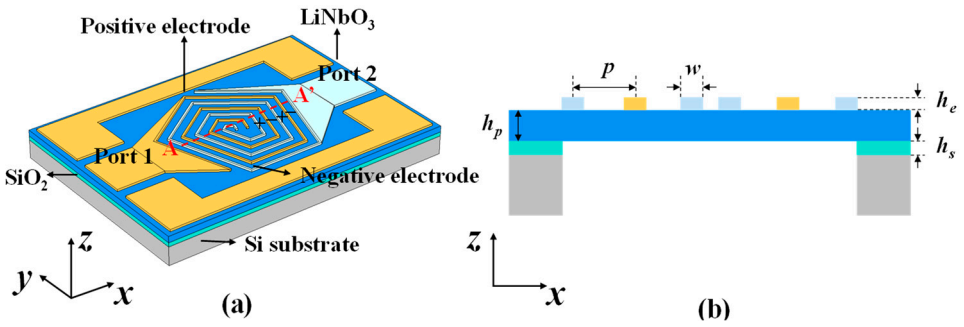

Figure 3. (**a**) Schematic drawing of XBAR with pentagon spiral shape electrode. (**b**) The A-A′ cross-section view of the resonator.

The finite element simulation is carried out to further analyze the performance of the resonator with pentagon spiral electrodes. The thickness of the Z-cut $LiNbO_3$ thin film (h_p) and electrode (h_e) is set to 330 nm and 200 nm, respectively, to achieve a 5.4 GHz resonant frequency (f_s), as shown in Figure 4a. The width of electrodes (w) is defined as 1 µm and the pitch (p) equals to 5 µm. Figure 4b shows the horizontal displacement distribution at resonance frequency along the A-A′ cross-section of the resonator with pentagon spiral electrodes and shows the horizontal displacement deformation in the B-B′ cross-section. The horizontal displacement is antisymmetric with the centre plane of the wave excited in the piezoelectric layer, which corresponds to the standard A_1 mode acoustic wave [20,21]. The proposed pentagon spiral-shaped electrodes applying alternating voltage can excite the electrical fields along both the x-direction and y-direction, thus exciting A_1 mode shear wave along both x- and y-directions, utilizing both the e_{24} and e_{15} piezoelectric constants [19]. However, the K^2_{eff} of structure with pentagon spiral-shaped electrodes is not improved relative to that of IDTs structure, which may be owing to the piezoelectric coefficient being e_{24} equal to e_{15}, and no superposition effect occurs. Furthermore, we investigate the influence of the electrode rotation angle in respect to x-direction and the influence of p on the K^2_{eff}.

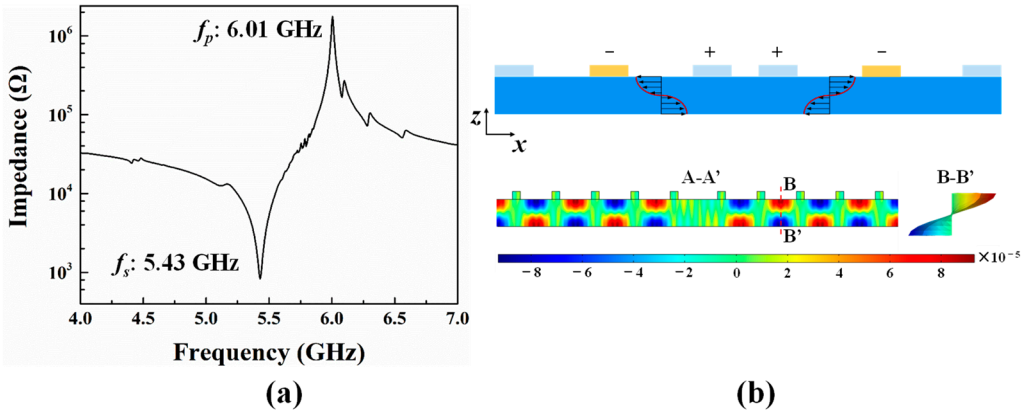

Figure 4. (**a**) The simulated impedance curve of resonator with pentagon spiral electrodes. (**b**) The simulated horizontal displacement mode shape at resonance frequency of A_1 mode along the A-A′ cross section and the horizontal displacement deformation in the B-B′ cross section.

First, we investigate the effect of electrode rotation angle in respect to x-direction with Z-cut $LiNbO_3$ plate on K^2_{eff}. The K^2_{eff} of XBAR can be obtained by the approximated Formulas (2) and (3) [22–24]. It can be concluded that the K^2_{eff} is positive to piezoelectric coefficient e_{15} of Z-cut $LiNbO_3$ thin film. The simulated K^2_{eff} vs. different rotation angle is depicted in Figure 5. The K^2_{eff} of the XBAR is maintained around 23.5% as the rotation angle of electrodes increases from 0° to 180°, which may contribute to the equality of the e_{24} and e_{15} of Z-cut $LiNbO_3$.

$$K^2_{eff} = \frac{K^2}{1+K^2} = \frac{\pi^2}{4} \times \frac{(f_p - f_s)}{f_p}, \tag{3}$$

$$K^2 = \frac{e^2_{15}}{\varepsilon_r \varepsilon_0 C_{44}}, \tag{4}$$

where the f_s and f_p are the resonance and anti-resonance frequency of the resonator, e_{15} is the piezoelectric coefficient of the $LiNbO_3$ thin film, ε_r and ε_0 are the relative permittivity and vacuum permittivity, and C_{44} is the elastic constant of the $LiNbO_3$ thin film.

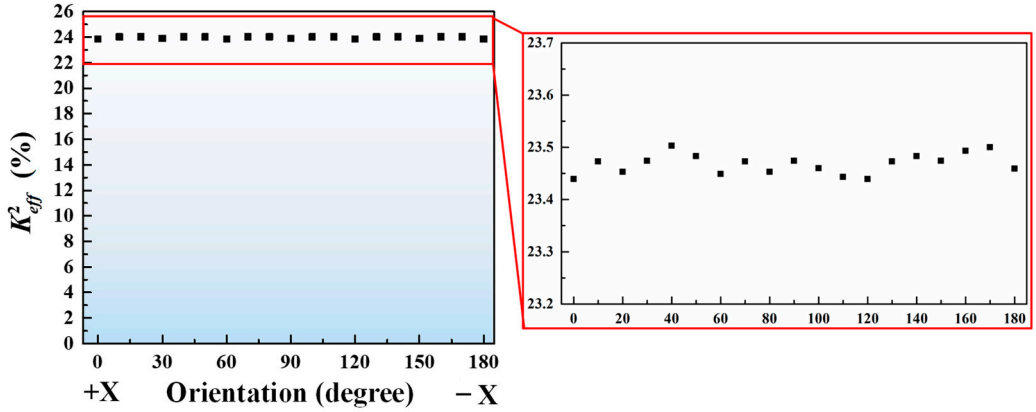

Figure 5. Calculated electromechanical coupling efficient of the A_1 mode acoustic wave in a Z-cut LiNbO3 thin film vs. the rotation angle of electrodes.

By simplifying the classic dispersion equation for anti-symmetric A_1 mode and using h_p/p as a small parameter, we can obtain the approximate dispersion Equation (5) [25]. More precisely, for practical design of XBARs, it is advised to use the empirical Formula (6) [26].

$$\frac{\Delta\omega}{\omega_s} = \left(\frac{h_p}{p}\right)^2 \times \left\{\frac{1}{2} + \frac{8}{\pi} \times \frac{V_T}{V_L} \times \frac{1}{\tan\left(\pi \frac{h_p}{\lambda_L}\right)}\right\}, \tag{5}$$

$$\frac{\Delta\omega}{\omega_s} = C1 \times \frac{h_p}{p} + C2 \times \left(\frac{h_p}{p}\right)^2. \tag{6}$$

Here, $\omega_s = 2\pi f_s$ is the angular frequency of resonator. The first term "1/2" in brackets corresponds to simple "shear wave in rectangular resonator" model, while the second term shows that longitudinal component of Lamb wave does matter. The λ_L is the wavelength of longitudinal bulk wave dependent on frequency. $C1$ and $C2$ are constants for linear and quadratic coefficients. According to the empirical Formula (4), we describe the relationship between $\Delta\omega/\omega_s$ and h_p/p. It can be deduced from Formula (5) and Figure 6 that $\Delta\omega/\omega_s$ is negatively correlated with p, which indicates that the decrease of K^2_{eff} with the increase of p as h_p is the same.

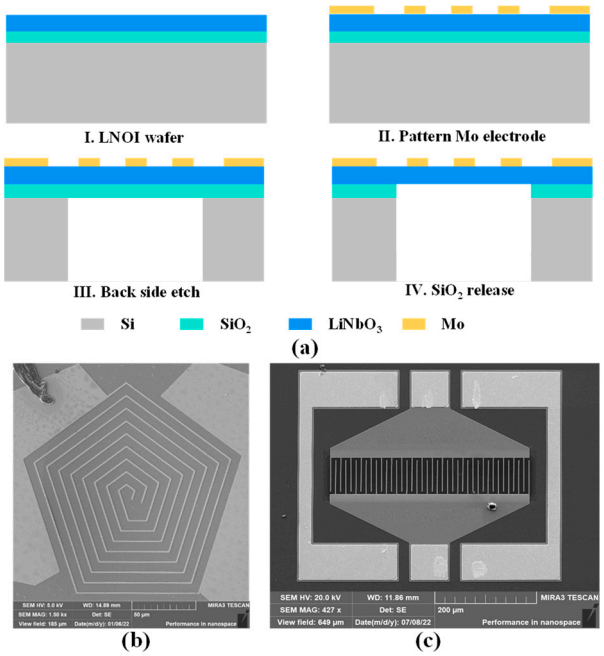

Figure 6. (**a**) Fabrication process flow for our resonator. I. Cross-section view of the LNOI wafer. II. Mo electrode pattern on the surface of $LiNbO_3$. III. Backside Si deep reactive-ion etch. IV. Wet etch of buried SiO_2 layer. (**b**) SEM image of the fabricated device with pentagon spiral electrodes. (**c**) SEM image of the fabricated device with IDEs.

3. Fabrication and Results

A series of XBARs, utilizing pentagon spiral electrodes with varied p and utilizing IDEs, have been fabricated. The fabrication process of resonator is shown in Figure 6a. The substrate wafer consisted of 330 nm-thick Z-cut $LiNbO_3$ thin film, 2 µm-thick SiO_2 and Si substrate, which is provided by NanoLN. Inc. First, 200 nm Mo thin film is deposited on the surface of $LiNbO_3$ thin film and patterned as pentagon spiral shape or IDEs by lithography and reactive ion etching technology. Then, 300 nm-thick SiO_2 is deposited on the surface of $LiNbO_3$ and Mo thin film by Plasma Enhanced Chemical Vapor Deposition (PECVD) as protective layer. Subsequently, $LiNbO_3$ thin film release is performed with backside Si deep reactive-ion etch (DRIE) process, followed by a wet etch with hydrofluoric acid solution to remove the buried SiO_2 layer underneath the piezoelectric membrane. By exactly controlling the release time, the resonators with suspended working area only are realized. The scanning electron microscope (SEM) images of the fabricated devices with pentagon spiral shape and IDEs are shown in Figure 6b,c.

The scattering (S) parameter measurements are carried out using Keysight Network Analyzer (N5222B) connecting to a Cascade Microtech's GSG probe station. Prior to the measurement, the setup is properly calibrated to remove the contribution of the probes and the cabling and only measure the ensemble of pads plus resonators. Figure 7 shows the experimentally obtained impedance curves vs. frequency of resonators with IDEs and pentagon spiral electrodes. The parameters of both resonators with IDEs and pentagon spiral electrodes are the same. The thickness of the Z-cut $LiNbO_3$ thin film (h_p) and electrode (h_e) is set to 330 nm and 200 nm, respectively. The width of electrodes (w) is defined as 1 µm and the pitch (p) equals to 5 µm. The resonance frequency of XBAR with IDTs and pentagon spiral electrodes is 5.38 and 5.43 GHz, and K^2_{eff} is 22.5% and 21.3%, respectively. The K^2_{eff} of the resonator with pentagon spiral electrodes is almost equal to that of IDTs, which demonstrates that the electrode rotation angle has no impact on K^2_{eff} of XBAR on Z-cut $LiNbO_3$ thin film. Furthermore, it is also worth mentioning that the spurious modes in the impedance curve of XBAR with pentagon spiral electrodes are obviously suppressed, while the curve of resonator with IDEs structure is disturbed by spurious modes. In XBAR

with IDE structure, the transverse waves are reflected at the edge of the electrode and form standing waves, thus causing spurious modes. However, in XBAR with pentagon spiral structure, due to the non-parallelism of electrode edges, the transverse waves have different reflection path at each point on the electrode edge, and the propagation path becomes longer, as shown in Figure 7b. When the transverse wave propagates through a long path, the energy of the standing wave is attenuated very low; therefore, the amplitude of spurious modes on the impedance curve are greatly reduced. It can also be noticed that the quality factor of XBAR with pentagon spiral electrodes is lower than that of XBAR with IDEs. The length of pentagon spiral electrodes is much larger than that of IDEs, which will increase the resistant of electrodes and eventually increase the electrical loss of electrodes.

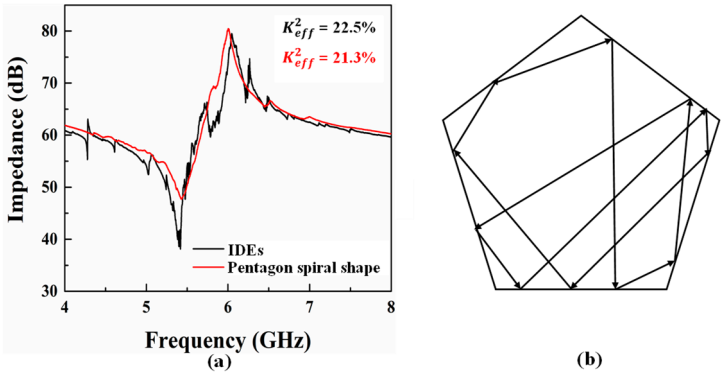

Figure 7. (**a**) The measured impedance curve of XBARs with IDTs structure (black) and pentagon spiral electrodes (red) vs. frequency, respectively. (**b**) Schematic diagram of acoustic wave propagation path in a pentagonal electrode.

Figure 8a shows the measured impedance curves of XBARs with different p of the top pentagon spiral electrodes. The resonance frequency is 5.433 GHz, 5.432 GHz and 5.230 GHz, respectively, when the p of electrodes is 5, 10 and 20 µm. The measured resonance frequency of the resonator with p = 20 µm is lower than that of p = 5 and 10 µm, which may due to the in-plane thickness inhomogeneity of $LiNbO_3$ thin film, where the standing A_1 modes are thickness-dependent when $h_p \ll p$. As p increases from 5 µm to 20 µm, the measured K^2_{eff} decreases from 21.3% to 15.8% gradually as shown in Figure 8b. To better understand the variation of the K^2_{eff} with different p, we adopt Berlincour's Formulations (7) and (8) for electromechanical coupling calculation, which can be expressed as [27–29]

$$K^2 = \frac{U_m^2}{U_e U_d}, \tag{7}$$

$$U_m \propto \int (E.d.T)\, dV, \tag{8}$$

where K^2 is the electromechanical coupling, U_m, U_d, and U_e are the mutual energy, electrical energy, and elastic energy. E, d, T and V are the electric field, the piezoelectric coefficient, stress, and volume of the piezoelectric material, respectively. Equation (7) signifies the importance of the overlap between the applied electric field and the stress distribution of the resonant mode inside the piezoelectric material in the thickness direction. Figures 9 and 10 show the stress distribution and total displacement distribution of A_1 mode in the thickness direction of the $LiNbO_3$ thin film, as the p = 5, 8, 10, 16 and 20 µm, respectively. The stress distribution and total displacement distribution declines with the increase of p, indicating the decrease in mutual energy and finally causing the diminution of K^2_{eff}.

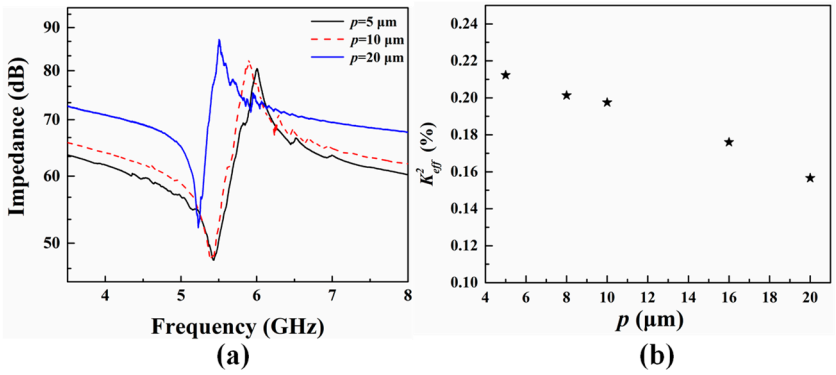

Figure 8. The measured impedance curve and K_{eff}^2 with different pitch (p). (**a**) The measured impedance curve of resonator with different pitch (p). (**b**) The measured K_{eff}^2 vs. different pitch (p).

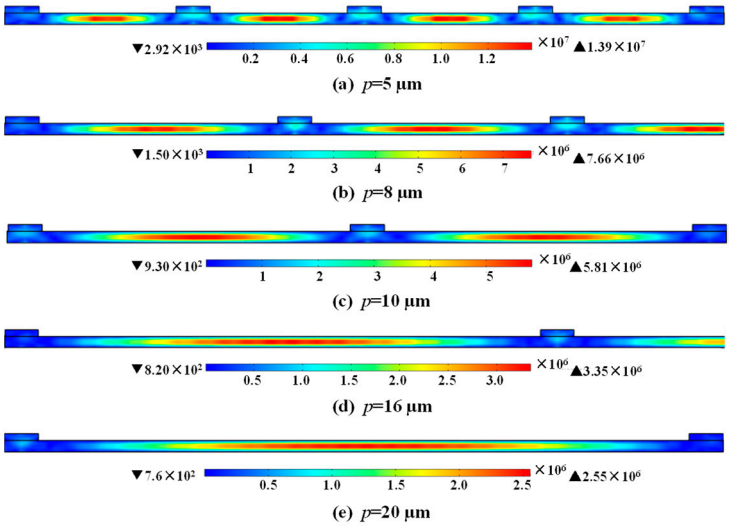

Figure 9. The simulated stress distribution at resonance as (**a**) p = 5 μm, (**b**) p = 8 μm, (**c**) p = 10 μm, (**d**) p = 16 μm and (**e**) p = 20 μm, while the width of electrode is maintained at 1 μm.

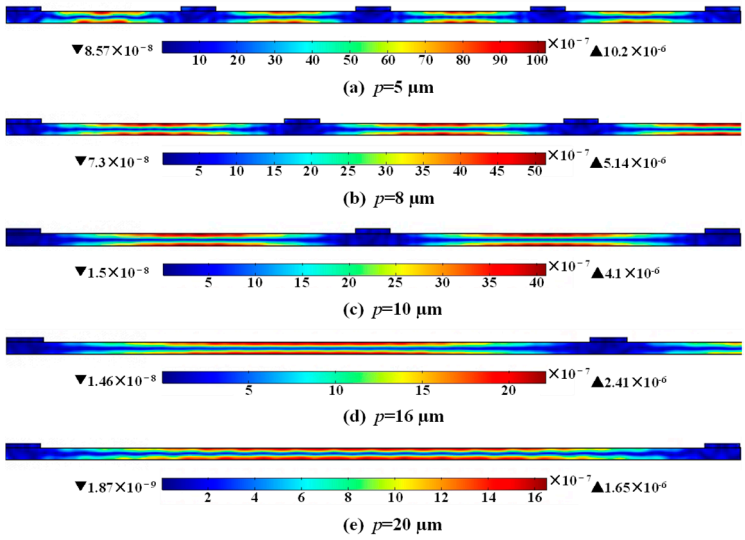

Figure 10. The simulated displacement distribution at resonance as (**a**) p = 5 μm, (**b**) p = 8 μm, (**c**) p = 10 μm, (**d**) p = 16 μm and (**e**) p = 20 μm, while the width of electrode is maintained at 1 μm.

4. Conclusions

In conclusion, we design and fabricate XBARs with pentagon spiral shape electrodes based on Z-cut $LiNbO_3$ thin films. The proposed structure realized an A_1 mode shear wave at 5.433 GHz along with K^2_{eff} of 21.3%. The thickness of $LiNbO_3$ thin film and the rotation angle of electrodes have no impact on the K^2_{eff} of the proposed resonator. However, the K^2_{eff} of XBAR is affected by the p of electrodes, decreasing from 21.3% to 15.8% with the increasement of p from 5 to 20 µm. Finally, a XBAR operates at 5.43 GHz with K^2_{eff} of 21.5%, and little spurious mode is obtained when w = 1 µm and p = 5 µm. The almost no spurious mode resonator has great potential for 50 Ω impedance match within a miniature size applied in super high-frequency RF front-end filters.

Author Contributions: Conceptualization, Y.X.; methodology, Y.X.; investigation, Y.X.; resources, Z.W.; data curation, T.L.; writing—original draft preparation, Y.X.; writ-ing—review and editing, W.L. and Y.C.; visualization, Y.C.; supervision, C.S.; project administration, Y.L.; funding acquisi-tion, Y.L. All authors have read and agreed to the published version of the manuscript.

Funding: This work was supported by National Key R&D Program of China (No. 2020YFB2008803) and the Young Scientists Fund of the National Natural Science Foundation of China (Grant No. 62201405).

Conflicts of Interest: The authors declare no conflict of interest.

References

1. Ruppel, C.C.W. Acoustic Wave Filter Technology–A Review. *IEEE Trans. Ultrason. Ferroelectr. Freq. Control.* **2017**, *64*, 1390–1400. [CrossRef] [PubMed]
2. Popovski, P.; Trillingsgaard, K.F.; Simeone, O.; Durisi, G. 5G Wireless Network Slicing for eMBB, URLLC, and mMTC: A Communication-Theoretic View. *IEEE Access* **2018**, *6*, 55765–55779. [CrossRef]
3. Lee, J.; Tejedor, E.; Ranta-aho, K.; Wang, H.; Lee, K.T.; Semaan, E.; Mohyeldin, E.; Song, J.; Bergljung, C.; Jung, S. Spectrum for 5G: Global Status, Challenges, and Enabling Technologies. *IEEE Commun. Mag.* **2018**, *56*, 12–18. [CrossRef]
4. Takai, T.; Iwamoto, H.; Takamine, Y.; Fuyutsume, T.; Nakao, T.; Hiramoto, M.; Toi, T.; Koshino, M.I.H.P. SAW technology and its application to microacoustic components (Invited). In Proceedings of the 2017 IEEE International Ultrasonics Symposium (IUS), Washington, DC, USA, 6–9 September 2017; pp. 1–8.
5. Aigner, R.; Fattinger, G.; Schaefer, M.; Karnati, K.; Rothemund, R.; Dumont, F. BAW Filters for 5G Bands. In Proceedings of the 2018 IEEE International Electron Devices Meeting (IEDM), San Francisco, CA, USA, 1–5 December 2018; pp. 14.15.11–14.15.14.
6. Liu, Y.; Cai, Y.; Zhang, Y.; Tovstopyat, A.; Liu, S.; Sun, C. Materials, Design, and Characteristics of Bulk Acoustic Wave Resonator: A Review. *Micromachines* **2020**, *11*, 630. [CrossRef] [PubMed]
7. Koskela, J.; Plessky, V.P.; Willemsen, B.A.; Turner, P.J.; Garcia, B.; Hammond, R.B.; Fenzi, N.O. Fast GPU-Assisted FEM Simulations of 3D Periodic TCSAW, IHP, and XBAR Devices. In Proceedings of the 2019 IEEE International Ultrasonics Symposium (IUS), Glasgow, UK, 6–9 October 2019; pp. 181–184.
8. Koulakis, J.; Koskela, J.; Yang, W.; Myers, L.; Dyer, G.; Garcia, B. XBAR physics and next generation filter design. In Proceedings of the 2021 IEEE International Ultrasonics Symposium (IUS), Virtual Symposium, 11–16 September 2021; pp. 1–5.
9. Faizan, M.; Pastina, A.D.; Yandrapalli, S.; Turner, P.J.; Hammond, R.B.; Plessky, V.; Villanueva, L.G. Fabrication Of Lithium Niobate Bulk Acoustic Resonator For 5G Filters. In Proceedings of the 2019 20th International Conference on Solid-State Sensors, Actuators and Microsystems & Eurosensors XXXIII (TRANSDUCERS & EUROSENSORS XXXIII), Berlin, Germany, 23–27 June 2019; pp. 1752–1755.
10. Yang, Y.; Gao, A.; Lu, R.; Gong, S. 5 Ghz lithium niobate MEMS resonators with high FoM of 153. In Proceedings of the 2017 IEEE 30th International Conference on Micro Electro Mechanical Systems (MEMS), Las Vegas, NV, USA, 22–26 January 2017; pp. 942–945.
11. Gong, S.; Piazza, G. Laterally vibrating lithium niobate MEMS resonators with high electromechanical coupling and Quality factor. In Proceedings of the 2012 IEEE International Ultrasonics Symposium, Dresden, Germany, 7–10 October 2012; pp. 1051–1054.
12. Plessky, V.; Yandrapalli, S.; Turner, P.J.; Villanueva, L.G.; Koskela, J.; Faizan, M.; Pastina, A.D.; Garcia, B.; Costa, J.; Hammond, R.B. Laterally excited bulk wave resonators (XBARs) based on thin Lithium Niobate platelet for 5GHz and 13 GHz filters. In Proceedings of the 2019 IEEE MTT-S International Microwave Symposium (IMS), Los Angeles, CA, USA, 2–7 June 2019; pp. 512–515.
13. Lu, R.; Yang, Y.; Link, S.; Gong, S. A1 Resonators in 128° Y-cut Lithium Niobate with Electromechanical Coupling of 46.4%. *J. Microelectromechan. Syst.* **2020**, *29*, 313–319. [CrossRef]
14. Peng, B.; Hu, N.; Jia, B.; Wang, H. A novel N79 filter using solid-mounted A1-mode resonator for 5G applications. In Proceedings of the 2021 IEEE International Ultrasonics Symposium (IUS), Virtual Symposium, 11–16 September 2021; pp. 1–4.

15. Gong, S.; Piazza, G. Large frequency tuning of Lithium Niobate laterally vibrating MEMS resonators via electric boundary reconfiguration. In Proceedings of the 2013 Transducers & Eurosensors XXVII: The 17th International Conference on Solid-State Sensors, Actuators and Microsystems (TRANSDUCERS & EUROSENSORS XXVII), Barcelona, Spain, 16–20 June 2013; pp. 2465–2468.
16. Zou, J.; Yantchev, V.; Iliev, F.; Plessky, V.; Samadian, S.; Hammond, R.B.; Turner, P.J. Ultra-Large-Coupling and Spurious-Free SH_0 Plate Acoustic Wave Resonators Based on Thin $LiNbO_3$. *IEEE Trans. Ultrason. Ferroelectr. Freq. Control.* **2020**, *67*, 374–386. [CrossRef] [PubMed]
17. Adler, E.L. Electromechanical coupling to Lamb and shear-horizontal modes in piezoelectric plates. *IEEE Trans. Ultrason. Ferroelectr. Freq. Control.* **1989**, *36*, 223–230. [CrossRef] [PubMed]
18. Kuypers, J.H.; Pisano, A.P. Green's function analysis of Lamb wave resonators. In Proceedings of the 2008 IEEE Ultrasonics Symposium, Beijing, China, 2–5 November 2008; pp. 1548–1551.
19. Zou, J.; Iliev, F.; Hammond, R.B.; Samadian, S.; Thorvaldsson, T.; Turner, P.J.; Yantchev, V.; Fenzi, N.O.; Plessky, V. Design of Ultra-Large-Coupling SH0 Plate Wave Resonators on LiNbO3 with Clean Spectrum. In Proceedings of the 2019 Joint Conference of the IEEE International Frequency Control Symposium and European Frequency and Time Forum (EFTF/IFC), Orlando, FL, USA, 14–18 April 2019; pp. 1–6.
20. Lu, R.; Li, M.H.; Yang, Y.; Manzaneque, T.; Gong, S. Accurate Extraction of Large Electromechanical Coupling in Piezoelectric MEMS Resonators. *J. Microelectromechan. Syst.* **2019**, *28*, 209–218. [CrossRef]
21. Zou, Y.; Nian, L.; Cai, Y.; Liu, Y.; Tovstopyat, A.; Liu, W.; Sun, C. Dual-mode thin film bulk acoustic wave resonator and filter. *J. Appl. Phys.* **2020**, *128*, 194503. [CrossRef]
22. Plessky, V.; Küçük, S.; Yandrapalli, S.; Villanueva, L.G. A formula for the admittance of laterally excited bulk wave resonators (XBARs). *Electron. Lett.* **2021**, *57*, 773–775. [CrossRef]
23. Yang, Y.; Lu, R.; Manzaneque, T.; Gong, S. Toward Ka Band Acoustics: Lithium Niobate Asymmetrical Mode Piezoelectric MEMS Resonators. In Proceedings of the 2018 IEEE International Frequency Control Symposium (IFCS), Olympic Valley, CA, USA, 21–24 May 2018; pp. 1–5.
24. Yandrapalli, S.; Eroglu, S.E.K.; Plessky, V.; Atakan, H.B.; Villanueva, L.G. Study of Thin Film $LiNbO_3$ Laterally Excited Bulk Acoustic Resonators. *J. Microelectromechan. Syst.* **2022**, *31*, 217–225. [CrossRef]
25. Barnett, D.M.; Lothe, J. Dislocations and line charges in anisotropic piezoelectric insulators. *Phys. Status Solidi (b)* **1975**, *67*, 105–111. [CrossRef]
26. Plessky, V.; Yandrapalli, S.; Küçük, S.; Villanueva, L.G. Resonance Frequency Dependence Of A1 Lamb Mode On The Pitch Of The Electrode Structure. In Proceedings of the 2021 Joint Conference of the European Frequency and Time Forum and IEEE International Frequency Control Symposium (EFTF/IFCS), Virtual Symposium, 7–17 July 2021; pp. 1–3.
27. Hassanien, A.E.; Gong, S. An Acoustic Resonator with Electromechanical Coupling of 16% and Low TCF at 5.4 GHz. In Proceedings of the 2021 IEEE International Ultrasonics Symposium (IUS), Virtual Symposium, 11–16 September 2021; pp. 1–4.
28. Hassanien, A.E.; Lu, R.; Gong, S. A Near Zero TCF Acoustic Resonator with High Electromechanical Coupling of 13.5% at 3.5 GHz. In Proceedings of the 2021 IEEE MTT-S International Microwave Symposium (IMS), Los Angeles, CA, USA, 7–25 June 2021; pp. 218–221.
29. Hassanien, A.E.; Lu, R.; Gong, S. Near-Zero Drift and High Electromechanical Coupling Acoustic Resonators at > 3.5 GHz. *IEEE Trans. Microw. Theory Tech.* **2021**, *69*, 3706–3714. [CrossRef]